Article:
Xu, S, Yang, L orcid.org/0000-0003-0935-3921, Liu, Y-Z et al. (3 more authors) (2020) Boosting hydrogen evolution performance by using a plasma-sputtered porous monolithic W2C@WC1−x/Mo film electrocatalyst. Journal of Materials Chemistry A, 8 (37). pp. 19473-19483. ISSN 2050-7488

https://doi.org/10.1039/d0ta05251e

Boosting Hydrogen Evolution Performance by Plasma-Sputtered Porous Monolithic $W_2C@WC_{1-x}$/Mo Film Electrocatalyst

Shusheng Xu [a, b]*, Liuquan Yang [a], Yu-Zhen Liu [c], Yong Hua [a], Xiaoming Gao [b], Anne Neville [a,]*

[a] *Institute of Functional Surfaces, School of Mechanical Engineering, University of Leeds, Leeds, LS2 9JT, UK*
[b] *State Key Laboratory of Solid Lubrication, Lanzhou Institute of Chemical Physics, Chinese Academy of Sciences, Lanzhou 730000, People's Republic of China*
[c] *Centre for Nano-Wear, School of Mechanical Engineering, Yonsei University, Seoul 03722, Republic of Korea*
**Corresponding author:*
E-mail address (Anne Neville): a.neville@leeds.ac.uk
E-mail address (Shusheng Xu): sxshiting@gmail.com

Electronic Supplementary Information (ESI) available.

The establishment of an efficient and economic mean of producing hydrogen *via* the electrocatalytic water-splitting will facilitate the extensive commercialization of fuel cells, and the round-the-clock model of electrocatalytic hydrogen production will alleviate the intermittency issue in associated with the sustainable energy sources. To enable this feature of renewable hydrogen energy, the key point is to develop cheap, large-scale and high-performance hydrogen evolution electrocatalysts as an alternative to noble metals. Here, a simple and robust physically-sputtering strategy is reported to massively prepare the porous and defect-enriched $W_2C@WC_{1-x}$ film electrocatalyst on carbon cloth (CC) in the W, C and Ar ions plasma atmosphere. The preferential re-sputtering mechanism promotes the loss of activated W and C ions in plasma and extracts more C from plasma, resulting in the ultimate formation of the defective $W_2C@WC_{1-x}$ film. The ratio of W_2C to WC_{1-x} increased and the particle size decreased when the additional nano-scale thickness Mo sublayers were further incorporated. The monolithic and porous $W_2C@WC_{1-x}$/Mo multilayer film as binder-free electrocatalyst on flexible CC is created. It exhibits excellent HER performance with a low overpotential of 58 mV *vs.* RHE to drive a current density of -10 $mA{\cdot}cm^{-2}$, a low Tafel slope of 41 $mV{\cdot}dec^{-1}$ and over 6 days' long-term running stability in the 0.5 M H_2SO_4 solution. It outperforms most of the recently-reported outstanding non-noble metal electrocatalysts. This work sheds a light on a new route to regulate the tungsten-carbide catalyst morphology and composition with aim to boost its HER activity.

1. Introduction

Hydrogen (H_2), as a clean and sustainable energy carrier, is a promising alternative to the traditional fossil fuels due to its high energy density and the characteristics of zero-emission of global warming gases from their ultilization [1,2]. An economical and effective method for large-scale hydrogen production is electrochemical water-splitting by using renewable electrical energy when an electrocatalyst on the reactive electrode is employed [3-9]. Currently, the most efficient electrocatalysts to reduce the dynamic overpotential for the hydrogen evolution reaction (HER) are noble metals, e.g. platinum (Pt), with high activity. However, their low earth-abundance and high cost hampers large-scale utilization [8-12]. Therefore, extensive efforts have been dedicated to develop the low-cost and earth-aboundant non-noble-metal HER catalysts to replace Pt for the urgent need of practical applications.

The transition metal based compounds (e.g., Mo_2C [9,13,14], W_2C [9,15], WC [16,17], MoN [18-20]) have emerged as inexpensive alteratives to the noble metals for HER. Mo_xC and W_xC have attracted intense interest due to their Pt-like electronic feature (originating from the donation of electrons from carbon to the Mo and W 5*d* orbits [21-24], as proved by density functional theoretical (DFT) calculation results), chemical inertness, strong metal-support interactions and low cost [25,26]. Specifically, the recent reports demonstrated clearly that W_2C is a more active electrocatalyst for HER than WC because it has a less negative Gibbs free energy (ΔG_H) of hydrogen adsorption and higher electronic density of states (DOS) at the Fermi level [9,15,27]. Construction of tungsten carbide

electrocatalysts with well-defined nanostructures is critical for achieving excellent HER performance. Over the past few years, multiple fabrication techniques emerged for the production of W_2C, such as multistep wet-chemistry synthesis from precursor/high temperature sintering and pyrolysis [16,17,28-33], and chemical systhesis in active vapor environments [34-36]. However, it has inferior electrical conductivity which limits the whole electrocatalytic performance of HER. The excellent HER activity of W_2C electrocatalyst can be demonstrated when they are further coupled with the precious carbon nanotubes (CNT) [15,34], graphitic C_3N_4 [37,38], and nitrogen-doped graphene oxide (N-rGO) [39-42] to expose much more active surface area, and improve the electron transport properties and chemical stability.

The common synthesis approaches of W_2C nanoparticles in liquid conditions present large challenges of unavoidable excessive growth of crystal, and the high temperature all-solid-state synthetic strategy leads to easy aggregation of W_2C nanoparticles [29,43]. They both decrease in the number of exposed active sites. Moreover, for the as-prepared nanoparticles robustly adhere to the current collector, inactive polymer binders are added that lead to shielding of the partial active sites and an increase in the electrode resistance. Electrocatalyst synthesis strategy beyond the aforementioned traditional methods have received little attention. Of note, the chemical vapor deposition (CVD) method for preparing additive-free 2D transition metal compounds has been reported, but the yield of CVD is extremely low. The physical vapor deposition (PVD) approach was also employed to synthesize the HER catalysts [44, 45]. On basis of the aforementioned, developing a simple and robust strategy which could be applied at a large-scale for the additive-free carbide electrode electrocatalyst with high performance is still required to enable its practical application and reach the full level of exploitation for HER.

Herein, we propose a one-step physically-sputtering strategy to fabricate the large-scale and porous tungsten carbide on a supported carbon cloth (CC) in the plasma atmosphere. This process is scalable and intrinsically enables a low-cost processing method for manufacturing carbide-based electrocatalysts. Importantly, by aid of the preferential re-sputtering characteritics of the energetic W and C atoms via carefully-controlling the process parameters (Ar pressure, sputtering power source, and the substrate bias voltage), more C atoms can be extracted from the growing WC film, ultimately forming a highly active $W_2C@WC_{1-x}$ for HER. The complementary advantages of high activity of W_2C phase and superior electrical conductivity of the WC_{1-x} phase promoted the enhanced HER performance of the deposited $W_2C@WC_{1-x}$ film electrodes. The Mo possesses excellent electrical conductivity and can play the role on transporting the electron through the film electrocatalyst. Meanwhile, it has lower cost than the noble metal of Au, Ag etc.. As the additional ultrathin Mo sublayers with nano-scale thickness were incorporated into the porous $W_2C@WC_{1-x}$ matrix, the excessive growth of the W_2C and WC_{1-x} nanoparticles was hindered. Accordingly, the specific surface rate of $W_2C@WC_{1-x}$ matrix increased significantly. The HER performance of the $W_2C@WC_{1-x}$/Mo film electrode on flexible CC is excellent with a low overpotential of 58 mV *vs.* RHE at a current density of -10 $mA{\cdot}cm^{-2}$ and a low Tafel slope of 41 $mV{\cdot}dec^{-1}$ in 0.5 M H_2SO_4 solution, which are comparable to the most reported the best WC based electrocatalysts. Also, the electrodes possess excellent electrochemical performance stability at the current densities of ~22 $mA{\cdot}cm^{-2}$ (lab-grade) and ~110 $mA{\cdot}cm^{-2}$ (industry-grade). The HER activity and stability of the $W_2C@WC_{1-x}$/Mo film on CC outperformed the most of the reported non-noble-metal electrocatalysts. More importantly, this novel, innovative and scalable strategy can transform hydrogen-evolution catalyst production and provide an economical solution for the industrial H_2 production processes at large current density. This strategy might be a potential extension to other electrocatalysts.

2. Experimental Section

The porous and additive-free $W_2C@WC_{1-x}$ films on CC were deposited *via* one-step magnetron sputtering technology in the Ar plasma chamber (Hauzer, Flexicoat 850). The maximum area of the deposited film relies on the size of original WC and Mo targets. Here, both the 99.99% WC and 99.99% Mo plane targets are 600 mm × 125 mm × 12 mm in size. The CC substrates were generally cleaned by actone for 10 minutes, alcohol for 10 minutes and deionized water (DI) for 5 minutes to remove the adsorbates before the film deposition. The deposition conditions were under Ar pressure of 2.4 Pa, CC substrate bias voltage of -90 V, and sputtering powers of 6.0 kW of WC target and 2.0 kW of Mo target, respectively. The internal layout of the deposition system is shown in **Figure S1**. The designed film thickness depends on the deposition time as given in the following content.

The surface and cross-sectional morphologies of the $W_2C@WC_{1-x}$ films on CC were investigated by field emission scanning electron microscopy (FESEM, Hitachi SU8230) attached by energy-dispersive X-ray spectroscopy (EDS). The phase structure was charaterized by X-ray diffraction (XRD, Bruker D8) using Cu K_α radiation source. The nanostructure of the film was observed by a high-resolution transmission electron microscopy (HRTEM, FEI Titan Themis Cubed 300) attached by energy-dispersive X-ray spectroscopy (EDS). The chemical composition was analysed by X-ray photoelectron spectroscopy (XPS, Thermo UK).

Electrochemical measurements were performed using an electrochemical workstation (Ivium) in 0.5 M H_2SO_4 electrolyte. The Pt rod electrode, Ag/AgCl (3 mol/L KCl) electrode and $W_2C@WC_{1-x}$ loaded CC electrode were used as the counter, reference and working electrodes, respectively. Before the tests, the Ag/AgCl reference electrode was properly calibrated. The potentials, measured against the Ag/AgCl (3 mol/L KCl) electrode, were converted into the reversible hydrogen electrode (RHE) according to the equation of $E_{RHE}=E_{Ag/AgCl}+0.205+0.059\times pH$ V. Unless the specifically mentioned, all the electrochemical measurements were *iR*-uncompensated. The polarization curves were achieved by sweeping the potential from 0 to -0.25 V *vs.* RHE at a sweep rate of 5 $mV\cdot s^{-1}$. Tafel slopes were determined by fitting the linear region of the Tafel plots to the Tafel equation of $\eta=b\log(j)+a$ by replotting the polarization curves, where η is the overpotential, b is the Tafel slope, and *j* is the current density. The AC impedance was detected from 100, 000 Hz to 0.01 Hz with an amplitude of 10 mV at the overpotential of 100 mV. The main arcs of the electrochemical impedance spectroscopy (EIS) spectra were matched utilizing a simplified Randles equivalent circuit (REC) consisting of resistance (R_s) in series with a parallel arrangement of the constant phase element (CPE) and the charge-transfer resistance (R_{ct}). To estimate the relative electrochemically active surface areas of the deposited film, the cyclic voltammetry (CV) for double layer capacitance was tested under the potential window from 0.1 to 0.2 V *vs* RHE with various scan rates (10, 20, 30, 40, 50, 60, 70, 80 and 90 $mV\cdot s^{-1}$). The current-time responses were detected by chronoamperometric measurements at the overpotential of 90 mV (lab-grade) for 6 days, and 170 mV (Industry-grade to simulate the industrial H_2 production) for 52 hours, respectively. The tests were to address the long-term efficiency and answer how durable the new electrodes are.

3. Results and Discussion

The schematic illustration of the preparation process of $W_2C@WC_{1-x}$ and $W_2C@WC_{1-x}$/Mo film catalysts is presented in **Figure 1**a. Prior to the film deposition, the closed chamber (**Figure S1**) was firstly vacuumed (6.0×10^{-3} Pa). The Ar plasma formed in the chamber as the electrical power was applied on the target. The target materials can be sputtered by the active Ar plasma. The sputtered target particles can deposit on the substrate as the substrate was facing to the target surface. The deposited film composition and structure can be adjusted by the sputtering power, sputtering gas pressure, bias voltage on substrate, space between target and substrate surface. The pure WC target was sputtered for fabricating the $W_2C@WC_{1-x}$ film on CC. The carousel with attached CC substrate was rotating during sputtering process (**Figure S1**). The $W_2C@WC_{1-x}$ and Mo sublayers in the $W_2C@WC_{1-x}$/Mo film on CC were alternately deposited from the pure WC and Mo targets, respectively, as presented in **Figure 1**b. Previously, the WC films were used as a protective layer against wear, corrosion and oxidation in surface engineering [46-48]. For these applications, the requirement is the dense structure on a stiff substrate (**Figure S2**). However, in this application, a well-defined active electrocatalyst material was porous structure with an enhanced specific surface area [12,14,31]. To fabricate the porous $W_2C@WC_{1-x}$ film, the optimial physically-sputtering parameters were determined in this study: inert medium Ar pressure of 2.4 Pa, sputtering power of 6.0 kW of pure WC target and substrate bias voltage of -90 V. The mass loading of active material $W_2C@WC_{1-x}$ was easily controlled just by changing the sputtering time. **Figure 1**c and **Figure S3** show the FESEM image of $W_2C@WC_{1-x}$ film catalyst on CC with deposition time of 120 minutes (EDS mapping in **Figure S4**). The $W_2C@WC_{1-x}$ film exhibits a porous and columnar structure, which benefits from the energetic W and C ions that are created by the high sputtering power and high medium Ar pressure [49-51].

As compared to the previous dense film (**Figure S2**), this porous structure of $W_2C@WC_{1-x}$ film could increase the exposed active sites, and the concomitant pore channels enable the free access of electrolyte to the interior of the electrode and allow more active sites to contact with the electrolyte [12,52]. To further minimize the $W_2C@WC_{1-x}$ particle size and create more active sites and optimize the monothetic conductivity of the film catalyst, the additional ultrathin Mo sublayers were added on each $W_2C@WC_{1-x}$ sublayer to prevent the coalescenece of $W_2C@WC_{1-x}$ particles in the columnar through a strategy of the alternating sputtering of WC and Mo. The FESEM images of the surface and cross-sectional morpholoies of $W_2C@WC_{1-x}$/Mo film are shown in **Figure 1**d and e, respectively. It can be noted that the columnar characteritics of the $W_2C@WC_{1-x}$/Mo film are maintained. The EDS elemental mapping images (**Figure 1**f) confirmed that the W, Mo and C were distributed on the CC substrate. Generally, the compatibility between deposited $W_2C@WC_{1-x}$/Mo film and substrate materials, especially for this binder-free ceramic film on the flexible CC, is one issue that affects the interface bonding and the further HER performance stability. In this study, a 1000 times' bending test was performed to evaluate the adhesion performance of the porous films on the flexible CC substrate. The result confirmed that there was no indication of coating peeling from the CC substrate. It appears that the strong interface coupling of $W_2C@WC_{1-x}$/Mo film and CC substrate and low

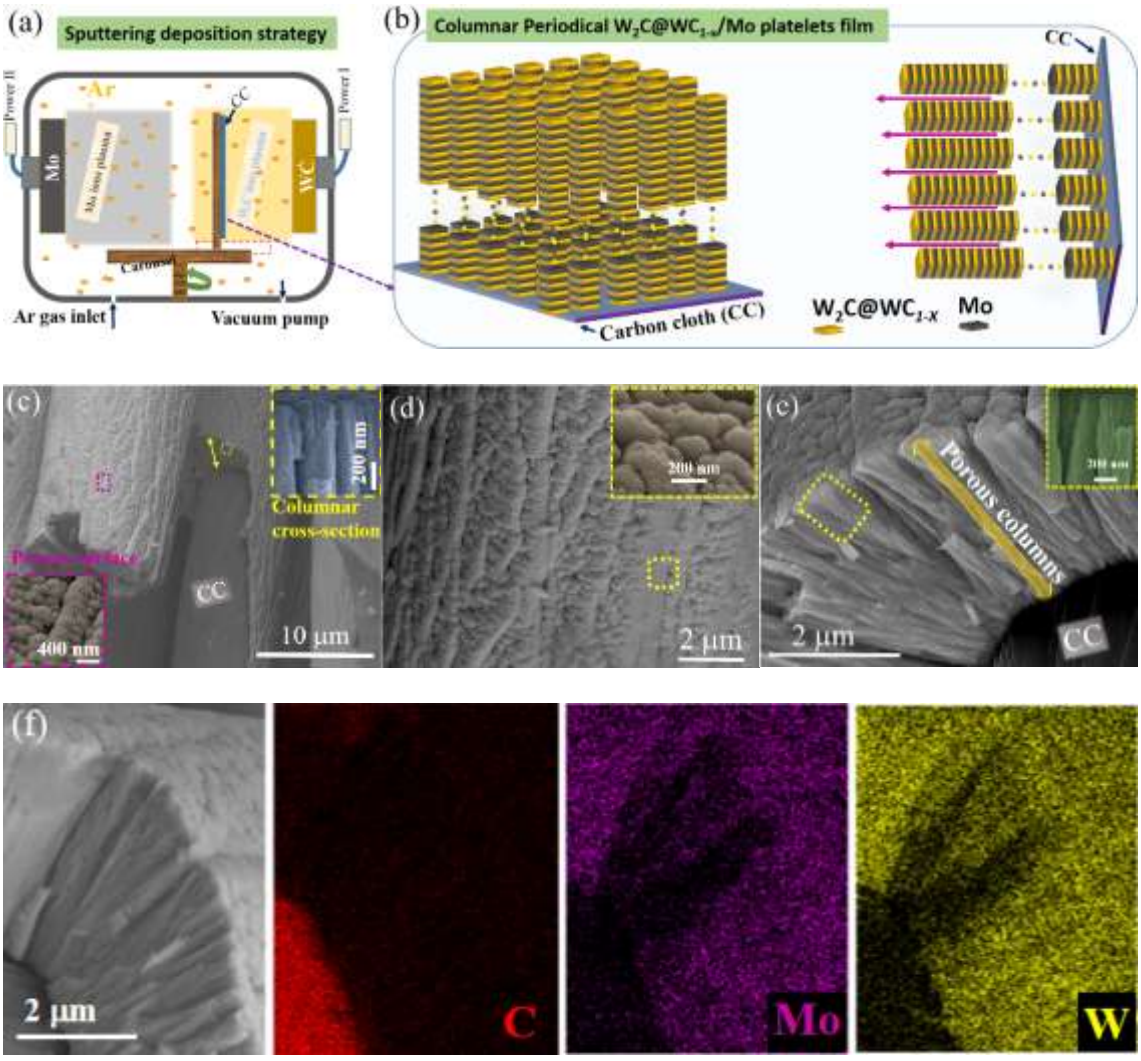

Figure 1. The illustrations of (a) the sputtering system for $W_2C@WC_{1-x}$ and $W_2C@WC_{1-x}$/Mo films on CC in Ar plasma atmosphere and (b) the porous and columnar structure of $W_2C@WC_{1-x}$/Mo film, the FESEM images (c) of the surface and cross-sectional morphologies of $W_2C@WC_{1-x}$ film on CC, (d) surface and (e) cross-sectional morphologies of $W_2C@WC_{1-x}$/Mo film on CC and (f) EDS elemental mappings of W, Mo and C of the cross-sectional $W_2C@WC_{1-x}$/Mo film on CC.

film internal stress, and the flexibility of the porous structure film maintains this interface integrity [53,54]. Moreover, this simple and robust preparation method of $W_2C@WC_{1-x}$/Mo film in Ar plasma chamber with size of Φ85 cm × 100 cm can yield about 1.1×10^4 cm^2 electrode (per batch), suggesting the feasibility of large-scale synthesis for electrocatalysts (**Figure S1**).

To characterize the morphology of the $W_2C@WC_{1-x}$ film and $W_2C@WC_{1-x}$/Mo multilayer film on CC, cross-section samples were made *via* FIB method (**Figure S5**). The cross-sectional morphologies can provide a complete understanding of the internal structural characteristics of the monolithic additive-free film. **Figure 2**a (and **Figure S6**) and **Figure S7**a show the HAAFD images of the cross-sectional $W_2C@WC_{1-x}$/Mo multilayer film and $W_2C@WC_{1-x}$ film, respectively. It can be seen that both films are comprised of columnar platelets (marked by the blue color) and the concominant pore channels (marked by the yellow color). The EDS mapping of W and Mo elements (in the insert of **Figure 2**a) shows that the monolithic $W_2C@WC_{1-x}$/Mo multilayer film was assembled by the alternating $W_2C@WC_{1-x}$ and Mo sublayers, but the incorporated thin Mo sublayers never hindered the formation of the columnar $W_2C@WC_{1-x}$/Mo platelets. This porous WC based structure for HER was firstly builded up in the high sputtering plasma environment by carefully controlling the deposition conditions.

We further characterized the nanostructure the $W_2C@WC_{1-x}$ and $W_2C@WC_{1-x}$/Mo multilayer films and the high resolution (HR)TEM images are shown in **Figure S7**b and **Figure 2**b, respectively. The columnar platelets in the $W_2C@WC_{1-x}$ film are composed of large nanocrystals with the size over 30 nm (**Figure S7**b). In comparison, the thickness of adjacent $W_2C@WC_{1-x}$ and Mo bilayers is 11.2 nm and each layer (in $W_2C@WC_{1-x}$ and Mo) was composed of nanocrystallite particles and a small quantity of amorphous phase (**Figure 2**b). The addition of ultrathin Mo sublayers (**Figure 2**b) appears to effectively prevent the $W_2C@WC_{1-x}$ from growing into the coarse crystallites. The $W_2C@WC_{1-x}$ nanocrystallites in the platelets possess particle sizes less than ~9 nm, resulting in an augmented specific surface area.

The films were further investigated by XPS to analyse the chemical components, as shown in **Figure 2**c. The atomic ratio of W/C is 0.62 as confirmed in the full-scan XPS spectrum of the $W_2C@WC_{1-x}$/Mo film, which is much lower than 1 (The stoichiometric ratio of the WC target is 1). The W/C ratio in the $W_2C@WC_{1-x}$ film also dropped to 0.73 (**Figure S8**a). It implies that C was selectively extracted by the preferential re-sputtering during the re-bonding process between W and C in the growing film in plasma. The loss of C in the $W_2C@WC_{1-x}$/Mo film is greater than in the $W_2C@WC_{1-x}$ film. The high-resolution W *4f* profile can be split into three pairs of peaks (**Figure 2**c). The fitting peaks at 31.6 eV and 33.7 eV can be assigned to features of W-C bonds in W_2C, while the doublet of 32.3 eV and 34.4 eV is attributed to the features of W-C bonds in WC_{1-x} [55,56]. Both WC_{1-x} and W_2C co-exist in the deposited $W_2C@WC_{1-x}$/Mo and $W_2C@WC_{1-x}$ films. However, the ratio of W_2C/WC_{1-x} is low in the $W_2C@WC_{1-x}$ film in comparison to the $W_2C@WC_{1-x}$/Mo film. The peaks located at 35.5eV and 37.6 eV are attributed to W^{6+}, which is corresponding to the oxide of WO_3, resulting from the inevitable surface oxidation of the film in air [17,29,55]. The high-resolution C *1s* profile can be split into three peaks. The main peak at 283.4 eV is indexed to the C-metal bonds, and the two peaks at 284.4 and 285.4 eV are attributed to sp^2 and sp^3 C-C bonds of contaminant carbon, respectively [57-59]. The peaks located at 228.3 eV and 231.4 eV (**Figure S9**) in high-resolution Mo *3d* profile are attributed to the metallic Mo sublayers in the $W_2C@WC_{1-x}$/Mo film [60]. Thus, the new compound species of $W_2C@WC_{1-x}$ in film can be prepared *via* the sputtering plasma approach that is substantially different to the original target compound (WC).

Figure 2d shows the XRD patterns of $W_2C@WC_{1-x}$ and $W_2C@WC_{1-x}$/Mo films on CC. The peak at ~25.8° is a feature of the carbon substrate (JCPDS No. 75-1621) and other peaks are assigned to WC_{1-x} and W_2C phases [61]. The three main diffraction peaks in the $W_2C@WC_{1-x}$/Mo film are indexed to (002), (040) and (240) planes of the W_2C crystal (JCPDS No. 20-1315), of which peaks are partially overlapped by peak groups of the WC_{1-x} (111) and W_2C (102) and Mo (112) and WC_{1-x} (200), and WC_{1-x} (220), and WC_{1-x} (311), respectively. The four main peaks in the $W_2C@WC_{1-x}$ film are indexed to (111), (220), (311) and (200) planes of the stable WC_{1-x} phase (JCPDS No. 20-1316), of which the first three peaks are partially overlapped by W_2C (002), W_2C (040) and W_2C (240), respectively [27,46,56-62]. These spectra further demonstrate that the active material of WC_{1-x} and W_2C phase compositions for HER have been successfully synthesized in the highly energetic W, C and Ar plasma environment. Furthermore, the W_2C is the dominant

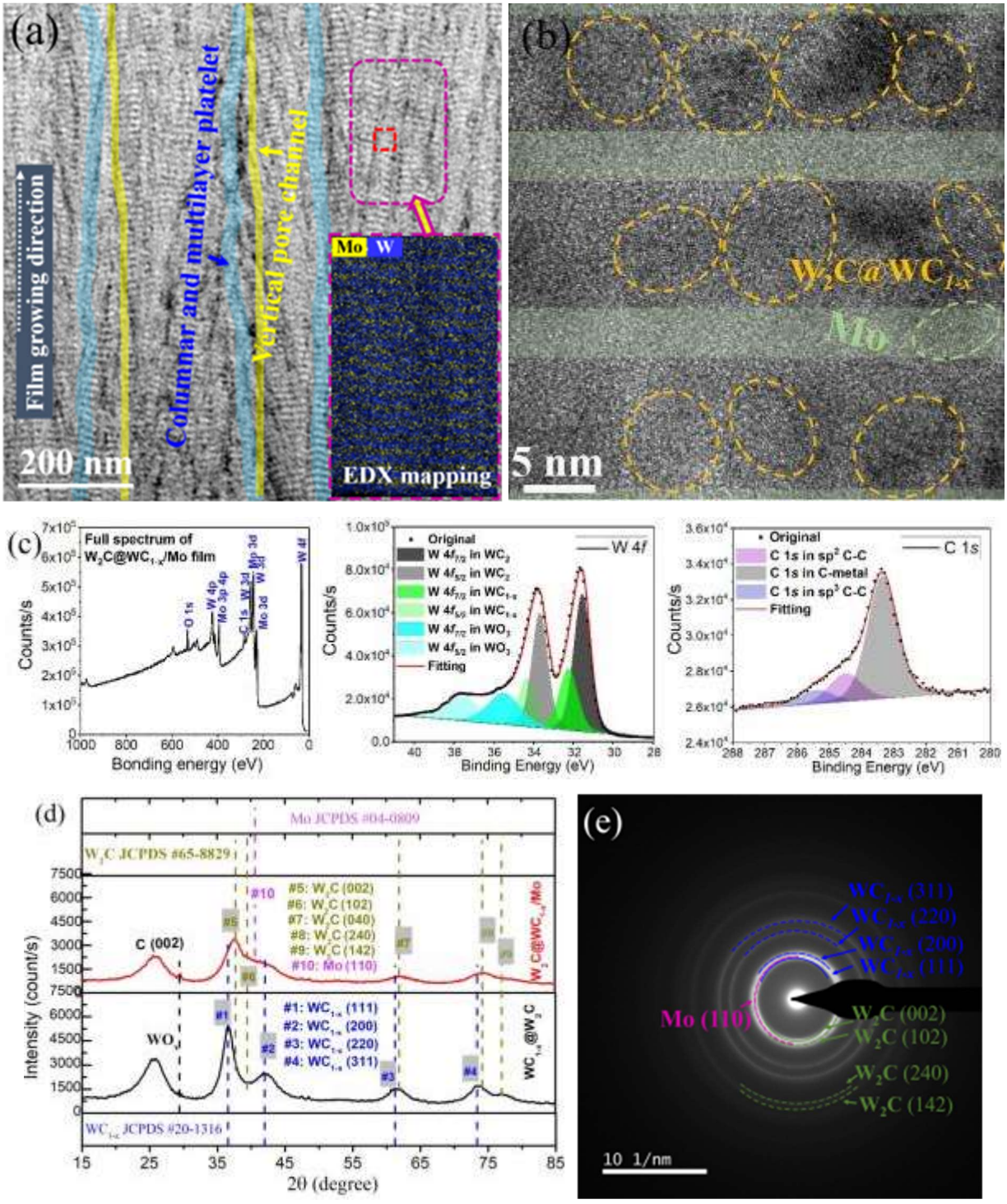

Figure 2. (a) HAAFD image of cross-sectional $W_2C@WC_{1-x}$/Mo multilayer film on CC with inserted EDX (Mo and W) elemental mappings, (b) HRTEM image of the representative zone from the selected red square in (a), (c) X-ray photoelectron survey of $W_2C@WC_{1-x}$/Mo multilayer and high-resolution spectra of W*4f* and C*1s*, (d) X-ray diffraction patterns of $W_2C@WC_{1-x}$/Mo multilayer and $W_2C@WC_{1-x}$ films, and (e) SAED of the representative zone in $W_2C@WC_{1-x}$/Mo multilayer film on CC.

nanocrystal composition in the $W_2C@WC_{1-x}$/Mo film but the WC_{1-x} is the dominant nanocrystal in the $W_2C@WC_{1-x}$ film. The crystal phase analysis results are in a good agreement with the XPS characterization of samples. As compared to the peaks in the $W_2C@WC_{1-x}$ film, the broadening of the diffraction peaks in the $W_2C@WC_{1-x}$/Mo film indicates the reduced size of carbide

nanoparticles, indicating that the excessive growth was hindered by the addition ultrathin sublayers of metallic Mo.

The selected area electron diffraction (SAED) patterns (as shown in **Figure 2**e and **Figure S10**) from the cross-sectional samples revealed the formation of $W_2C@WC_{1-x}$ nanoparticles and Mo nanoparticles. The blue patterns were indexed to the (311), (220), (200) and (111) planes of WC_{1-x} crystal phase, the green patterns were indexed to the (142), (240), (102) and (002) planes of W_2C crystal phase and the purple red pattern was indexed to the Mo (110) plane. The TEM-SAED results align with the aforementioned XRD characteritics of the $W_2C@WC_{1-x}$/Mo multilayer film. Meanwhile, its porous morphology is another advantage for electrocatalysis applications due to the open path enabling free access of the H^+-containing intermediate to the internal active sites of the electrode and free escape of the hydrogen product [12,52]. The incorporation of the ~3 nm Mo sublayers not only creates the high exposure ratio of internal $W_2C@WC_{1-x}$ nanoparticles in the film by blocking the growth of coarse WC crystallites, but also promotes the formation of the more active phase (W_2C) in the energetic plasma environment.

The ubiquitous preferential re-sputtering process during the growth of the film was the essential factor for the loss of W and C atoms and preferential extraction of C in the sputteirng plasam, as illustrated in **Figure 3**a. In the plasma atmosphere activated by the electric filed, the positively-charged Ar ions attracted the negative (WC) target, and the ejected W and C ions are deposited on the opposite (carbon cloth) substrate surface. As the electrical field is enhanced, a part of the ejected W and C ions became energetic and acted as the attackers to the growing carbide film, resulting in the re-sputtering of the WC film and the loss of the deposited species. Moreover, the preferential re-sputtering and scattering resulted in more C being extracted from the growing $W_2C@WC_{1-x}$ film [63-65]. The defects were ultimately formed in the $W_2C@WC_{1-x}$ particles (**Figure 3**b), which can act as efficient active sites for HER [66,67]. The atmosphere temperature increased to 190°C in the deposition chamber when the Mo target opposite was further activated for the $W_2C@WC_{1-x}$/Mo multilayer film deposition. In this case, the W and C ions became more energetic and the preferential re-sputtering of the growing film was further intensified, resulting in increase in the loss of C. We controlled the sputtering parameters carefully to achieve the aforementioned composition and morphology of the $W_2C@WC_{1-x}$/Mo electrocatalyst: (i) high plasma pressure of 2.4 Pa to create the porous morphology; (ii) high sputtering source density of 6.0 kW and moderate substrate bias voltage of -90 V to intensify the preferential sputtering of C in the growing film to create the defects; (iii) incorporation of ultrathin Mo sublayers to hinder the excessive growth of coarse crystallites of $W_2C@WC_{1-x}$; and (iv) increase in the atmosphere temperature of plasma by activating the additional Mo sputtering source target to promote more W_2C phase formation [61]. The vaporation-based deposition strategy is successfully developed for synthesising of the large-scale and porous electrocatalyst in this study (**Figure S1**).

The electrocatalytic HER activities of the film electrodes were evaluated under the 3-electrode configuration using N_2-saturated 0.5 M H_2SO_4 electrolyte. The mass loading of active material WC on CC is 2.34 mg cm^{-2}. The polarization curves were acquired from the iR-compensated linear sweep voltammetry measurements at 5 $mV{\cdot}s^{-1}$. **Figure 4**a and b present the polarization curves and the corresponding Tafel curves of different film electrocatalysts, respectively. The pristine conductive substrate CC itself shows a negligible activity of hydrogen-evolution, while the Pt exhibits excellent electrocatalytic activity with low overpotential of 46 mV $_{j=10\ mA{\cdot}cm^{-2}}$ and low Tafel slope of 34 $mV{\cdot}dec^{-1}$. The dense WC film exhibits a unremarkable and high overpotential of 219 mV $_{j=10\ mA{\cdot}cm^{-2}}$ and Tafel slope of 125 $mV{\cdot}dec^{-1}$. Once the dense film structure was modified into the porous and coarse WC column structure, it provides a reduced overpotential of 107 mV $_{j=10\ mA{\cdot}cm^{-2}}$ and Tafel slope of 72 $mV{\cdot}dec^{-1}$. This is much higher than those of the effective Pt. Interestingly, when the metallic Mo was incoporated into the WC matrix in the form of ~3 nm sublayers, a remarkable electrocatalytic activity of $W_2C@WC_{1-x}$/Mo film is achieved as low as 58 mV $_{j=10\ mA{\cdot}cm^{-2}}$ and a Tafel slope of 41 $mV{\cdot}dec^{-1}$. The values are higher than those of Pt, but they are very close to them. It indicates that the $W_2C@WC_{1-x}$/Mo film with the columnar structure could promote the HER electrocatalytic activity. The high value of Tafel slope of the dense $W_2C@WC_{1-x}$ film electrode suggests that the HER occurred *via* Volmer reaction mechanism wherein the surface coverage of adsorbed hydrogen (H_{ads}) on the electrode is the rate-dominating step (RDS) [52,68,69]. It should be due to the extremely low exposed surface of the internal $W_2C@WC_{1-x}$ particles in dense structure film. To enhance the high HER performance of WC based active materials, the desirable structure is composed of the high specific surface area of nanoparticles and high ratio of W_2C to WC_{1-x} in the porous electrode, where the RDS is the electrochemcial

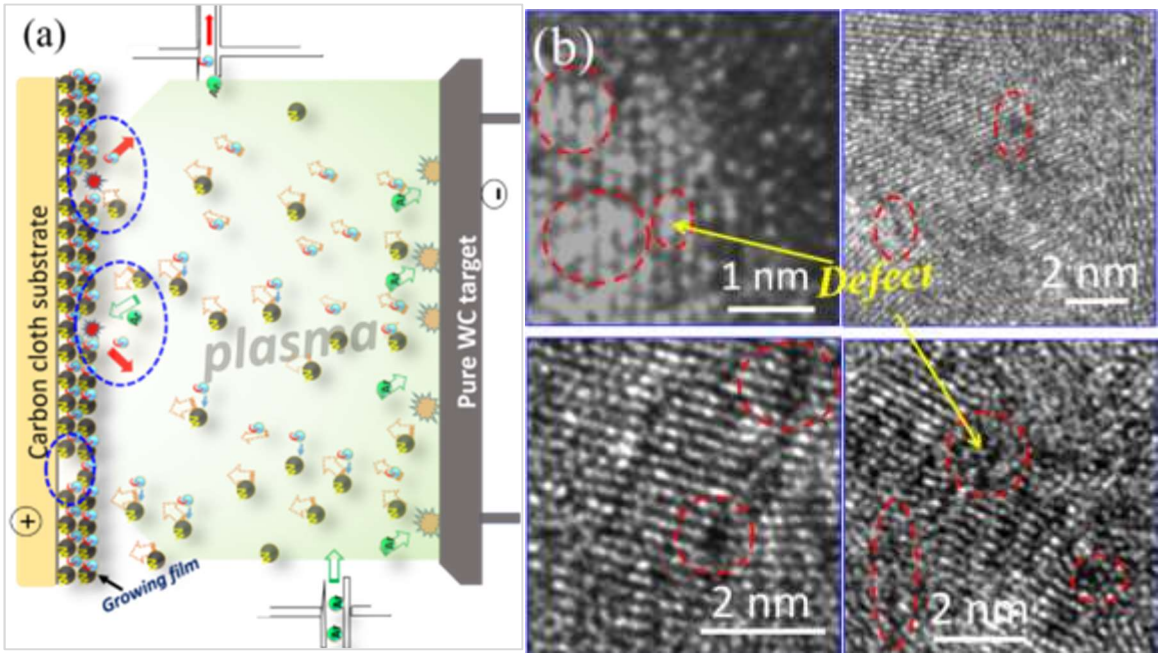

Figure 3 (a) The illustration of the re-sputtering mechanism during $W_2C@WC_{1-x}$ film growing process, and (b) the ultimately formed defective nanoparticles of $W_2C@WC_{1-x}$ in the multilayer film.

desorption dominated in the Volmer-Heyrovsky or Volmer-Tafel mechanism [52,69].

To further illustrate the origin of the HER kinetics, electrochemical impedance spectroscopy (EIS) was implemented at the overpotential of 100 mV *vs.* RHE, and the spectra are shown in **Figure 4**c. In the low frequency regime of the Nyquist plot, the semicircle appears but the Warburg impedance is absent, suggesting that surface exchange process of intermediate and the hydrogen product was the dominated step in HER process [52,70]. R_{ct} value of porous $W_2C@WC_{1-x}$/Mo (2.6 Ω) is lower than those of porous $W_2C@WC_{1-x}$ (4.2 Ω) and dense $W_2C@WC_{1-x}$ (7.3 Ω). The low resistance of $W_2C@WC_{1-x}$/Mo indicates the superior charge transport kinetics during the electrochemical process by improving the conductivity of porous electrocatalyst. This benefit can be related to the synergistic effect between the active material layer (W_2C and WC_{1-x}) and the metallic Mo sublayers that can reduce the electron transport resistance at the porous catalyst/electrolyte interface and then promote the fast HER reaction. It should be further emphasized that the increased specific surface area of size-reduced $W_2C@WC_{1-x}$ nanoparticles in the porous film plays a crucial roles on high HER activity. The electrochemical double-layer capacitance (C_{dl}) is considered to be linearly proportional to the relative surface area of the porous film, which was generally employed to study the activity in the HER [72,73]. Thus, the electrochemically active surface areas (ECSA) of films were investigated by measuring the C_{dl}, as shown in **Figure 4**d and **Figure S11**. Surprisingly, it can be seen that the C_{dl} of 64.3 $mF{\cdot}cm^{-2}$ presented by $W_2C@WC_{1-x}$ /Mo is superior to that of $W_2C@WC_{1-x}$ (31.6 $mF{\cdot}cm^{-2}$) and much higher than that of dense $W_2C@WC_{1-x}$ (9.8 $mF{\cdot}cm^{-2}$). It indicates that the $W_2C@WC_{1-x}$/Mo film possesses the highest electrochemical activity area, which should benefit from the columnar refinement of $W_2C@WC_{1-x}$ components as the conductive phase Mo sublayers were incorporated. The calculated TOF values of the dense $W_2C@WC_{1-x}$, culmnar $W_2C@WC_{1-x}$ and $W_2C@WC_{1-x}$/Mo film electrocatalysts (the inset of **Figure 4** d) are 0.101, 0.118 and 0.152 H_2 s^{-1}, respectively, at an overpotential of 200 mV. For comparison, the TOF values of molybdenum sulfide (the well known non-precious metal electrocatalyst for HER reaction) are presented, which is 1.4 H_2 s^{-1} for $MoS_{0.94}P_{0.53}$ [71] and 1.51 H_2 s^{-1} for se-MoS_2 [72] at an overpotential of 200 mV in 0.5 H_2SO_4 solution. It suggested that the intrinsic HER activity for the $W_2C@WC_{1-x}$ with more W_2C composition (**Figure 2** c,d) was enhanced in the

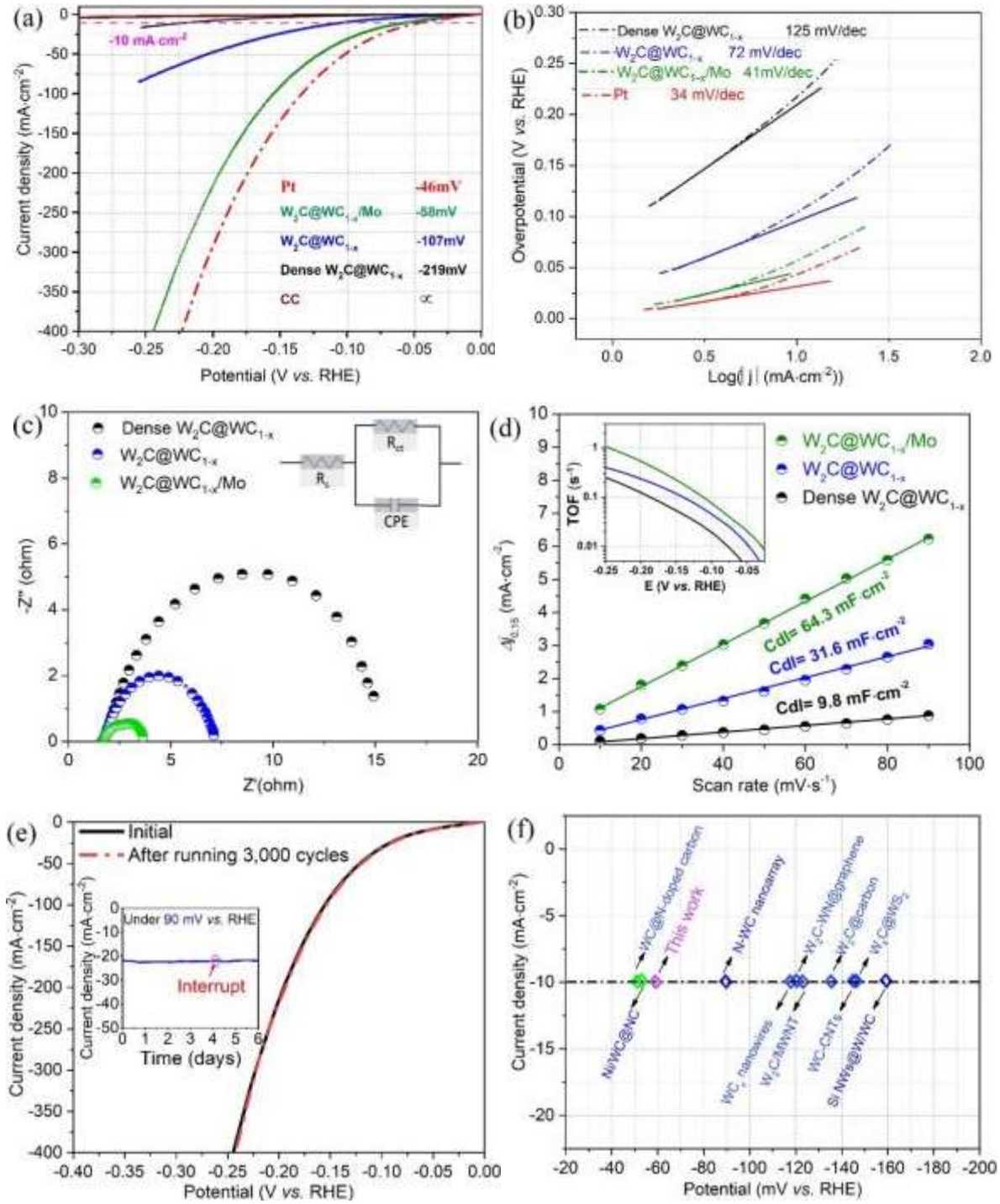

Figure 4 Performanes of $W_2C@WC_{1-x}$ film and $W_2C@WC_{1-x}$/Mo multilayer film as HER catalysts in 0.5 M H_2SO_4 solution: (a) Polarization curves of different film electrodes at 5 mV·s^{-1}. The mass loading of active material $W_2C@WC_{1-x}$ on CC is 2.34 mg·cm^{-2}. The pristine carbon cloth (CC) is also tested for comparison. (b) The corresponding Tafel slopes of active materials in (a). (c) The electrochemical impedance spectroscopy (EIS) Nyquist plots of the film electrodes at the overpotential of 100 mV *vs.* RHE. (d) Charge-current density difference plotted against the scan rate of the film electrodes. C_{dl} is equivalent to the half of the slope of the fitted line. Inset: TOF of film electrocatalyst within the Tafel region. (e) Polarization curves of the initial $W_2C@WC_{1-x}$/Mo and after running 3,000 cycles in 0.5 M H_2SO_4 solution at 5 mV·s^{-1}. Inset: Time-dependent current density curve of $W_2C@WC_{1-x}$/Mo under a static overpotential of 90 mV *vs.* RHE for 6 days (144 hours). (f) Comparison of the overpotentials to drive the current density of -10 mA·cm^{-2} of various tungsten carbides under acidic media. [15,17,29-31,33,34,42,58,72].

$W_2C@WC_{1-x}$/Mo electrocatalysts. In a word, the enhanced ECSA of porous film enhances the HER performance.

As a crucial evaluation for a HER catalyst, the electrocatalytic stability of the $W_2C@WC_{1-x}$/Mo film was assessed by long-time cycling and chronopotentiometry measurements. The results are displayed in **Figure 4**e. After running the working electrode for 3,000 cycles between 0 to -0.25 V *vs.* RHE at 5 $mV \cdot s^{-1}$, the polarization curve exhibits no loss of current density (**Figure 4**e). More importantly, the $W_2C@WC_{1-x}$/Mo electrode exhibits a 4.2% increase in current density after running for 6 days (144 hours) under a static overpotential of 90 mV *vs.* RHE in the chronopotentiometry test (inset in **Figure 4**e). The electrochemical performances of the film electrocatalysts were tested three times. The inter-reproducibility was great. This excellent stability of electrochemical performance at overpotential of 90 mV *vs.* RHE has never been reported for a WC based electrode. The current density skipped suddenly at the interruption moment of 96 hours, but it stabilized after the run-in stage.

To further simulate the industrial H_2 production process at large current density that might be interrupted, the HER stability test of $W_2C@WC_{1-x}$/Mo film was performed at 170 mV *vs.* RHE (**Figure S12**). At the interruption moments (running time of 7.2 and 28.2 hours), the transient of current density takes place but they could be stable again after the run-in stage. The final current density declines about 5.7% after 52 hours electrolysis of water. The transient of current density at the interrupting moments is related to the releasing of bubbles of cumulated H_2 from the film electrode pores [30,34,74]. **Figure 4**f presents a comparison with recently-reported tungsten carbide electrocatalysts under acidic media, determined by the overpotential to drive the current density of -10 $mA \cdot cm^{-2}$. Obviously, the overpotential of 58 mV observed on $W_2C@WC_{1-x}$/Mo film is comparable with that of the best W_2C/MWNT [15], WC@N-doped carbon [17] and Ni/WC@NC [29], and is much lower than that of N-WC nanoarray [30], WC_x nanowires [31], Si NWs@W/WC [33], WC-CNTs [34], W_2C-WN@graphene [42], $W_xC@WS_2$ [60] and W_2C@carbon [75].

For the $W_2C@WC_{1-x}$/Mo electrocatalyst after 3,000 sweeps between 0 to -0.25 V *vs.* RHE in 0.5 M H_2SO_4 solution, there is no obvious change of its FESEM image and XRD pattern (shown in **Figure S13** and **Figure 5**a) as compared to the fresh film electrocatalyst (**Figuer 1**d and **Figure 2**d), revealing the remarkable integrity of film structure. Furthermore, referred to the **Figure 2**c, the XPS spectra (**Figure 5**b and **Figure S14**) results also reveal that $W_2C@WC_{1-x}$/Mo retains its chemical composition stability. Thus, the $W_2C@WC_{1-x}$/Mo film on CC shows a competitive model for designing more promising HER electrocatalysts.

Previously, numerous density functional theory (DFT) calculations results have demonstrated that W 5*d* orbit would be broadened by hybridization between it and C *s*- and *p*- orbits (W_2C), resulting in the d-band state similar to that noble-metal-like Pt electrocatalyst [21-24,30,60,66]. Besides, the carbides of W show the Gibbs free energy (ΔG_{H^*}) of adsorbed hydrogen similar to Pt that is highly

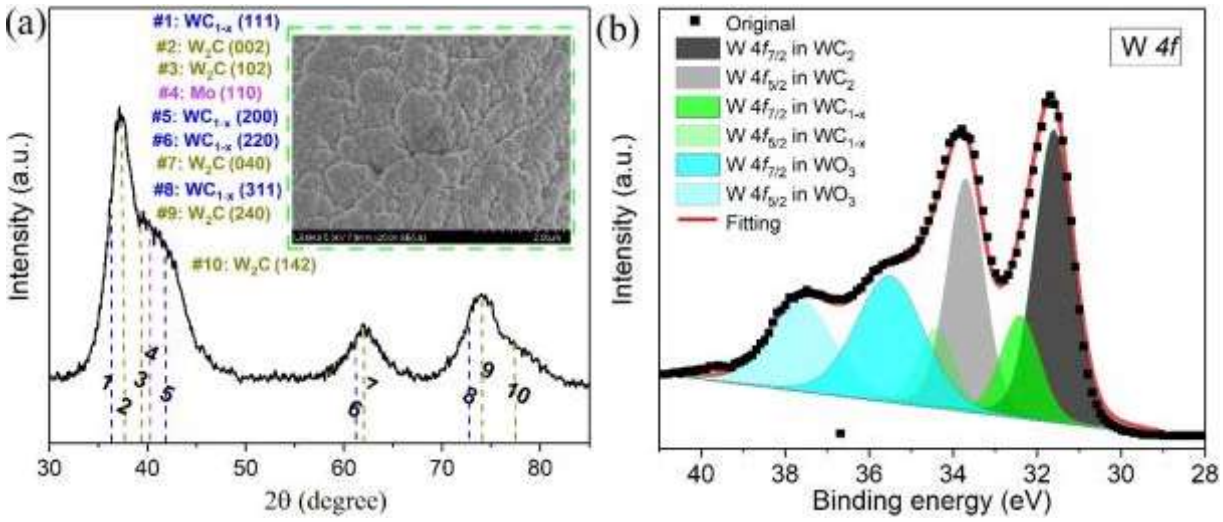

Figure 5 (a) The XRD pattern with the inserted FESEM image and (b) XPS of $W_2C@WC_{1-x}$/Mo film on CC after 3,000 sweeps between 0 to -0.25 V *vs.* RHE in 0.5 M H_2SO_4 solution.

active in acid solution. According to the aforementioned analyses in this study, the synergetic effects of essential factors, such as the more active phase of W_2C with low ΔG_{H^*}, increase in the electrochemical activity area with atomic-scale defects and the enhanced electrical conductivity, open channels enabling the internal active materials exposed to the electrolyte, all of them determined the high HER performance of the $W_2C@WC_{1-x}$/Mo electrode. Interestingly, as the substrate bias voltage of -90 V was increased to -1,000 V, the enhanced HER performance disappeared. This result suggests that the degree of extraction of carbon from the growing film by re-sputtering and preferential sputtering behaviours and the ultimately-formed local defect degree in $W_2C@WC_{1-x}$/Mo film electrodes should be carefully tailored, which are dominantly responsible for the enhanced HER performance.

4. Conclusion

In summary, we firstly demonstrated a highly efficient and robust $W_2C@WC_{1-x}$/Mo multilayer film on carbon cloth (CC) as a binder-free HER electrocatalyst electrode *via* the physically-sputtering technology. By aid of the physically preferential re-sputtering mechanism in the energetic plasma, a partial energetic W and C ions lost and extra C ions were extracted from the growing film, and ultimately the C-lacking and defect-enriched tungsten carbide formed, namely, $W_2C@WC_{1-x}$. The further incorporation of ~3 nm Mo sublayers could promote the more W_2C formation in the $W_2C@WC_{1-x}$/Mo in comparison to the $W_2C@WC_{1-x}$ film. The $W_2C@WC_{1-x}$/Mo film electrocatalyst exhibits excellent HER performance with a low overpotential of 58 mV *vs.* RHE at a current density of 10 $mA{\cdot}cm^{-2}$ and a low Tafel slope of 41 $mV{\cdot}dec^{-1}$ in 0.5 M H_2SO_4 solution, and superior long-term stability over 6 days' running without any decline. All these remarkable performances, together with novel deposition strategy of film on flexible CC substrate, are promoting for the industrial H_2 production in 0.5 M H_2SO_4 solution. This work shows a novel and facile constructing strategy of film electrode to explore more efficient tungsten carbides electrocatalysts.

Conflicts of interest

There are no conflicts to declare.

Acknowledgements

The authors are grateful for the financial support provided by Engineering and Physical Sciences Research Council (EPSRC, Grant No. EP/R00496X/1) in UK. We also would like to thank the helpful FIB and TEM tests by Mr. John Harrington, Mrs. Zebeada Aslam and Mr. Satuart Micklethwaite from Leeds Electron Microscopy and Spectroscopy Centre (LEMAS), University of Leeds.

Notes and references

1. J. A. Turner, *Science* **2004**, *305*, 972.
2. D. Voiry, H. S. Shin, K. P. Loh, M. Chhowalla, *Nat. Rev. Chem.* **2018**, *2*, 0105.
3. R. Subbaraman, D. Tripkovic, D. Strmcnik, K. C. Chang, M. Uchimura, A. P. Paulikas, V. Stamenkovic, N. M. Markovic, *Science* **2011**, *334*, 1256.
4. C. G. Morales-Guio, L. A. Stern, X. Hu, *Chem. Soc. Rev.* **2014**, *43*, 6555.
5. G. Chen, Z. W. Hu, Y. P. Zhu, B. B. Gu, Y. J. Zhong, H. J. Lin, C. T. Chen, W. Zhou, Z. P. Shao, *Adv. Mater.* **2018**, *30*, 1804333.
6. J. Hu, B. L. Huang, C. X. Zhang, Z. L. Wang, Y. M. An, D. Zhou, H. Lin, M. K. H. Leung, S. H. Yang, *Energy Environ. Sci.* **2017**, *10*, 593.
7. H. M. Yu, X. Yang, X. Xiao, M. Chen, Q. H. Zhang, L. Huang, J. B. Wu, T. Q. Li, S. M. Chen, L. Song, L. Gu, B. Y. Xia, G. Feng, J. Li, J. Zhou, *Adv. Mater.* **2018**, 30, 1805655.
8. X. X. Zou, Y. Zhang, *Chem. Soc. Rev.* **2015**, *44*, 5148.
9. Q. S. Gao, W. B. Zhang, Z. P. Shi, L. C. Yang, Y. Tang, *Adv. Mater.* **2019**, *31*, 1802880.
10. C. G. Morales-Guio, L. A. Stern, X. Hu, *Chem. Soc. Rev.* **2014**, *43*, 6555.
11. S. T. Hunt, M. Milina, Z. S. Wang, Y. Román-Leshkov, *Energy Environ. Sci.* **2016**, *9*, 3290.
12. S. Y. Nong, W. J. Dong, J. W. Yin, B. W. Dong, Y. Lu, X. T. Yuan, X. Wang, F. Q. Huang, *J. Am. Chem. Soc.* **2018**, *140*, 5719.
13. J. S. Li, Y. Wang, C. H. Liu, S. L. Li, Y. G. Wang, L. Z. Dong, Z. H. Dai, Y. F. Li, Y. Q. Lan, *Nat. Commun.* **2016**, *7*, 11204.
14. J. Jia, W. J. Zhou, Z. Q. Wei, T. L. Xiong, G. X. Li, L. L. Zhao, X. F. Zhang, H. Liu, J. Zhou, S. W. Chen, *Nano Energy* **2017**, *41*, 749-757.
15. Q. F. Gong, Y. Wang, Q. Hu, J. Zhou, R. F. Feng, P. N. Duchesne, P. Zhang, F. J. Chen, N. Han, Y. F. Li, C. H. Jin, Y. G. Li, S. T. Lee, *Nat. Commun.* **2016,** *7*, 13216.
16. S. T. Hunt, T. Nimmanwudipong, Y. Román-Leshkov, *Angew. Chem. Int. Ed.* **2014**, *53*, 5131.

17. Y. T. Xu, X. F. Xiao, Z. M. Ye, S. L. Zhao, R. G. Shen, C. T. He, J. P. Zhang, Y. D. Li, X. M. Chen, *J. Am. Chem. Soc.* **2017**,*139*, 5285-5288.
18. Y. P. Zhu, G. Chen, X. M. Xu, G. M. Yang, M. L. Liu, Z. P. Shao, *ACS Catal.* **2017**, *75*, 3540.
19. H. Y. Jin, X. Liu, Y. Jiao, A. Vasileff, Y. Zheng, S. Z. Qiao, *Nano Energy* **2018**, *53*, 690.
20. L. Ma, L. R. L. Ting, V. Molinari, C. Giordano, B. S. Yeo, *J. Mater. Chem. A* **2015**, *3*, 8361.
21. L. H. Bennett, J. R. Cuthill, A. J. McAlister, N. E. Erickson, R. E. Watson, *Science* **1974**, *184*, 563.
22. J. R. Kitchin, J. K. Nørskov, M. A. Barteau, J. G. Chen, *Catal. Today* **2005**, *105*, 66.
23. A. M. Alexander, J. S. Hargreaves, *Chem. Soc. Rev.* **2010**, *39*, 4388.
24. S. Y. Yao, X. Zhang, W. Zhou, R. Gao, W. Q. Xu, Y. F. Ye, L. L. Lin, X. D. Wen, P. Liu, B. B. Chen, E. Crumlin, J. H. Guo, Z. J. Zuo, W. Z. Li, J. L. Xie, L. Lu, C. J. Kiely, L. Gu, C. Shi, J. A. Rodriguez, D. Ma, *Science* **2017**, *357*, 389.
25. H. Vrubel, X. Hu, *Angew. Chem. Int. Ed.* **2012**, *51*, 12703.
26. M. Miao, J. Pan, T. He, Y. Yan, B. Y. Xia, X. Wang, *Chem. Eur. J. 2017*, *23*, 10947.
27. I. H. Kim, S. W. Park, D. W. Kim, *Nanoscale* **2018**, *10*, 21123.
28. Y. Shen, L. Li, J. Y. Xi, X. P. Qiu, *J. Mater. Chem. A* **2016**, *4*, 5817.
29. Y. Y. Ma, Z. L. Lang, L. K. Yan, Y. H. Wang, H. Q. Tan, K. Feng, Y. J. Xia, J. Zhong, Y. Liu, Z. H. Kang, Y.G. Li, *Energy Environ. Sci.* **2018**, *11*, 2114.
30. N. N. Han, K. R. Yang, Z. Y. Lu, Y. J. Li, W. W. Xu, T. F. Gao, Z. Cai, Y. Zhang, V. S. Batista, W. Liu, X. M. Sun, *Nat. Commun.* **2018**, *9*, 924.
31. B. W. Ren, D. Q. Li, Q. Y. Jin, H. Cui, C. X. Wang, ***J. Mater. Chem. A*** 2017, ***5***, 13196.
32. J. Zhu, K. Sakaushi, G. Clavel, M. Shalom, M. Antonietti, T.-P. Fellinger, *J. Am. Chem. Soc.* **2015**, *137*, 5480.
33. Z. K. Kou, T. T. Wang, Z. H. Pu, L. Wu, K. Xi, S. C. Mu, ***Nanoscale Horiz.*** 2019, *4*, 196-201.
34. X. J. Fan, H. Q. Zhou, X. Guo, *ACS Nano* **2015**, *9*, 5125.
35. D. R. Mohapatra, H. J. Lee, S. Sahoo, W. S. Lee, *CrystEngComm* **2012**, *14*, 2222.
36. M. Q. Zen, Y. X. Chen, J. X. Li, H. F. Xue, R. G. Mendes, J. X. Liu, T. Zhang, M. H. Rümmeli, L. Fu, *Nano Energy* **2017**, *33*, 356.
37. A. T. Garcia-Esparza , D. Cha , Y. Ou , J. Kubota , K. Domen, K. Takanabe, *ChemSusChem* **2013**, *6* , 168.
38. Y. Xiong, Y. P. Chen, N. Yang, C. D. Jin, Q. F. Sun, *Solar RRL* **2019**, *3*, 5.
39. J. Yang, Y. Xie, R. H. Wang, B. J. Jiang, C. G. Tian, G. Mu, J. Yin, B. Wang, H. G. Fu, *ACS Appl. Mater. Interfaces* **2013**, *14*, 6571.
40. L. P. Zhang, H. B. Yang, D. K. J. A. Wanigarathna, B. Liu, *Small Methods* **2018**, *2*, 1700353.
41. L. Chen, W. L. Chen, E. B. Wang, *J. Power Sources* **2018**, *380*, 18.
42. W. F. Chen, J. M. Schneider, K. Sasaki, C. H. Wang, J. Schneider, S. Iyer, Y. Zhu, J. T. Muckerman, E. Fujita, *ChemSusChem* **2014**, *7*, 2414.
43. B. Wang, G. Wang, H. Wang, *J. Mater. Chem. A* **2015**, *3*, 17403.
44. X. Zhang, Y. Zhang, B. B. Yu, X. L. Yin, W. J. Jiang, Y. Jiang, J. S. Hu, L. J. Wan, *J. Mater. Chem. A* **2015**, *3*, 19277.
45. *S. J. Rowley-Neale, M. Ratova, L. T. N. Fugita, G. C. Smith, A. Gaffar, J. Kulczyk-Malecka, P. J. Kelly, C. E. Banks, ACS Omega* **2018**, 3(*7*), 7235.
46. D. Q. He, J. B. Pu, L. P. Wang, G. A. Zhang, Y. X. Wang, Q. J. Xue, *Tribol Lett* **2016**, *63*, 14.
47. S. E. Mrabet, M. D. Abad, J. C. Sánchez-López, *Surf. Coat. Technol.* **2011**, *206*, 1913.
48. S. H. Ahn, J. H. Yoo, Y. S. Choi, J. G. Kim, J. G. Han, *Surf. Coat. Technol.* **2003**, *162*, 212.
49. J. A. Thornton, *J. Vac. Sci. Technol.* **1974**, *11*, 666.
50. O. Kluth, G. Schöpe, J. Hüpkes, C. Agashe, J. Müller, B. Rech, *Thin Solid Films* **2003**, *442*, 80.
51. S. S. Xu, X. M. Gao, M. Hu, J. Y. Sun, D. Jiang, F. Zhou, W. M. Liu, L. J. Weng, *Appl. Surf. Sci.* **2014**, *288*, 15.
52. D. McAteer , Z. Gholamvand , N. McEvoy, A. Harvey, E. O'Malley, G. S. Duesberg, J. N. Coleman, *ACS Nano* **2016**, *10*, 672-683.
53. J. A. Thornton, D. W. Hoffman, *Thin Solid Films* **1989**, *171*, 5.
54. A. Mani, P. Aubert, F. Mercier, H. Khodja, C. Berthier, P. Houdy, *Surf. Coat. Technol.* **2005**, *194*, 190.
55. L. N. Zhang, Y. Y. Ma, Z. L. Lang, Y. H. Wang, S. U. Khan, G. Yan, H. Q. Tan, H. Y. Zang, Y. G. Li, ***J. Mater. Chem. A*** 2018, *6*, 15395.
56. P. Xiao , X. Ge , H. Wang , Z. Liu , A. Fisher, X. Wang, *Adv. Funct. Mater.* **2015**, *25*, 1520.
57. J. Y. C. Qiu, Z. X. Yang, Q. Li, Y. Li, X. Wu, C. Y. Qi, Q. D. Qiao, ***J. Mater. Chem. A*** 2016, *4*, 13296.

58. L. F. Lin, M. Chen, L. M. Wu, *Adv. Mater. Interfaces* **2018**, *5*, 1801302.
59. S. S. Xu, Y. Z. Liu, M. Y. Gao, K. H. Kang, C. L. Kim, D. E. Kim, *Carbon* **2018**, *134*, 411.
60. F. M. Wang, P. He, Y. C. Li, T. A. Shifa, Y. Deng, K. L. Liu, Q. S. Wang, F. Wang, Y. Wen, Z. X. Wang, X. Y. Zhan, L. F. Sun, J. He, *Adv. Funct. Mater.* **2017**, *27*, 1605802.
61. Y. Gao, X. Y. Song, X. M. Liu, C. B. Wei, H. B. Wang, G. S. Guo, *Scripta Mater.* **2013**, *68*, 108;
62. J. E. Krzanowski, J. L. Endrino, *Mater. Lett.* **2004**, *58*, 3437.
63. H. L. Brown, S. A. Thornley, S. J. Wakeham, M. J. Thwaites, R. J. Curry, M. A. Baker, *J. Phys. D Appl. Phys.* **2015**, *48*, 335303.
64. K. Ellmer, *Phys. Stat. Sol. (b)* **2008**, *245*, 1745.
65. E. Särhammar, Sputtering and Characterization of Complex Multi-element Coatings, Thesis, *Uppsala University* **2014**.
66. B. You, X. Liu, G. X. Hu, S. Gul, J. Yano, D. E. Jiang, Y. J. Sun, *J. Am. Chem. Soc.* **2017**, *139*, 12283.
67. J. Staszak-Jirkovsky, C. D. Malliakas, P. P. Lopes, N. Danilovic, S. S. Kota, K. C. Chang, B. Genorio, D. Strmcnik, V. R. Stamenkovic, M. G. Kanatzidis, N. M. Markovic, *Nat. Mater.* **2016**, *15*, 197.
68. D. Voiry, J. U. Yang, M. Chhowalla, *Adv. Mater.* **2016**, *28*, 6197.
69. B. E. Conway, B. V. Tilak, *Electrochim. Acta* **2002**, *47*, 3571.
70. J. Hu, C. X. Zhang, L. Jiang, H. Lin, Y. M. An, D. Zhou, M. K. H. Leung, S. H. Yang, *Joule* **2017,** *1*, 383-393.
71. R. Q. Ye, P. del Angel-Vicente, Y. Y. Liu, M. J. Arellano-Jimenez, Z. W. Peng, T. Wang, Y. L. Li, B. I. Yakobson, S. H. Wei, M. J. Yacaman, J. M. Tour, *Adv. Mater.* **2016**, *28*, 1427.
72. J. Hu, B. L. Huang, C. X. Zhang, Z. L. Wang, Y. M. An, D. Zhou, H. Lin, M. K. H. Leung, S. H. Yang, *Energy Environ. Sci.* **2017**, *10*, 593.
73. Y. H. Huang, Y. H. Sun, X. L. Zheng, T. Aoki, B. Pattengale, J. E. Huang, X. He, W. Bian, S. Younan, N. Williams, J. Hu, J. X. Ge, N. Pu, X. X. Yan, X. Q. Pan, L. J. Zhang, Y. G. Wei, J. Gu, *Nat. Commun.* **2019**, *10*, 982.
74. M. Jiang, H. Wang, Y. J. Li, H. C. Zhang, G. X. Zhang, Z. Y. Lu, X. M. Sun, L. Jiang, *Small* **2017**, *13*, 1602240.
75. Y. Zhou, R. G. Ma, P. X. Li, Y. F. Chen, Q. Liu, G. Z. Cao, J. C. Wang, *J. Mater. Chem. A* **2016**, *4*, 8204.

Graphical Abstrate